

Phase Transition Kinetics of MAPbI₃ for Tetragonal-to-Orthorhombic Evolution

Jiawei Wu,[†] Jianfu Chen,[†] and Haifeng Wang*



Cite This: *JACS Au* 2023, 3, 1205–1212



Read Online

ACCESS |



Metrics & More



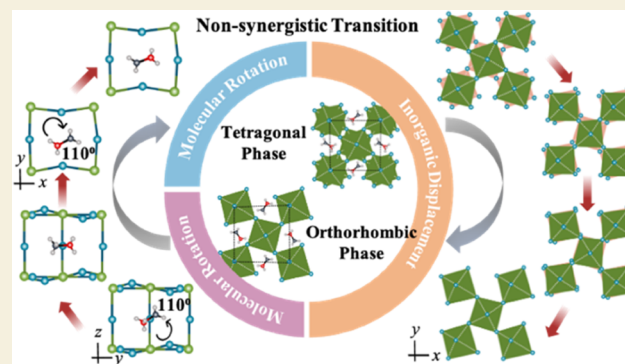
Article Recommendations



Supporting Information

ABSTRACT: Despite the commonly observed phase-instability-induced photovoltaic degradation of MAPbI₃, the phase transition kinetics at the atomic level remains elusive. Herein, by developing a stepwise NEB method, we clarify a nonsynergistic minimum-energy pathway for the tetragonal-to-orthorhombic phase transition. It is kinetically driven by the tilting of PbI₆⁴⁻ that induces a spontaneous small rotation of adjoining MA⁺ and ends with stepwise ~110° reorientations of two nonadjacent MA⁺ enabled by the cavity expansion. Compared to the common concerted mechanism, this process gives a low barrier of 0.08 eV/unit, demonstrating the easiness of the transition at extremely low temperatures and the importance of rotational entropies in regulating transition at elevated temperatures. With an explicit phase transition mechanism, we explore the structure-induced property response and reveal that introducing even low content of large-sized organic cations could help maintain the quasi-stable low-temperature performance of MAPbI₃ solar cells.

KEYWORDS: hybrid organic–inorganic perovskite, phase transition kinetics, photovoltaic efficiency, molecular reorientation, molecular switch



INTRODUCTION

MAPbI₃ as the champion material of hybrid organic–inorganic perovskites (HOIPs) has attracted widespread attention due to the low production cost and high photovoltaic efficiency. Despite the great progress in device efficiencies well over 25.7% in recent decades,^{1–5} the commercialization of this material remains limited due to the stability issue.^{6–10} In particular, tetragonal MAPbI₃ exhibits long photoexcited carrier lifetimes and diffusion length and has increasing photovoltaic applications; upon cooling below 160 K, it unfortunately undergoes a tetragonal-to-orthorhombic phase (TP-to-OP) transition and exhibits weakened solar cell performance.^{11–14} However, the origin of this temperature-dependent phase instability and structural evolution mechanism at such a low temperature are elusive due to the complexity of potential energy surface (PES), which involves an intramolecular or axial rotation of organic cations and subtle H-bond interactions with inorganic cages.^{15–20} In comparison with the all-inorganic perovskite, such a mixed relaxation nature gives extra complexity to locating the phase-transition minimum-energy path (MEP).

Toward such a challenging issue, more than one study has made great efforts to reveal the phase transition mechanism of HOIPs and generally emphasized the entropy effect in driving the transition at elevated temperatures, despite that the fact may be changed with decreasing temperatures;^{13,21–30} however, for the specific structural transition process, diverse views were

reported for different HOIPs, mainly focusing on the driving force of the tilting of PbI₆⁴⁻ octahedron,²¹ the rotation of MA⁺ cations,^{14,25} or the collective mode where organic and inorganic ions move together to drive the phase transition.²⁶ To the best of our knowledge, the definitive structural transition mechanism with full kinetic information included has been studied less, and it remains open on the competing of the rotation/vibration entropy contribution and transition kinetics with temperatures, which is crucial for understanding and balancing the material instability and photovoltaic performance. Thus, it is of general essence to unveil the minimum-energy phase evolution process and the kinetically rate-limiting factor at the atomic scale.

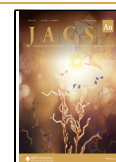
Noticeably, Chen et al. gave a possible transition pathway generated via the interpolation by monotonically changing reaction coordinates from the cubic to the hexagonal phase of FAPbI₃.²⁷ Such a strategy may likely neglect some possible nonsynergistic modes and result in the overestimation of transition barriers. In this regard, it calls for a more efficient method, allowing multipath sampling to locate the more

Received: February 5, 2023

Revised: March 7, 2023

Accepted: March 14, 2023

Published: March 23, 2023



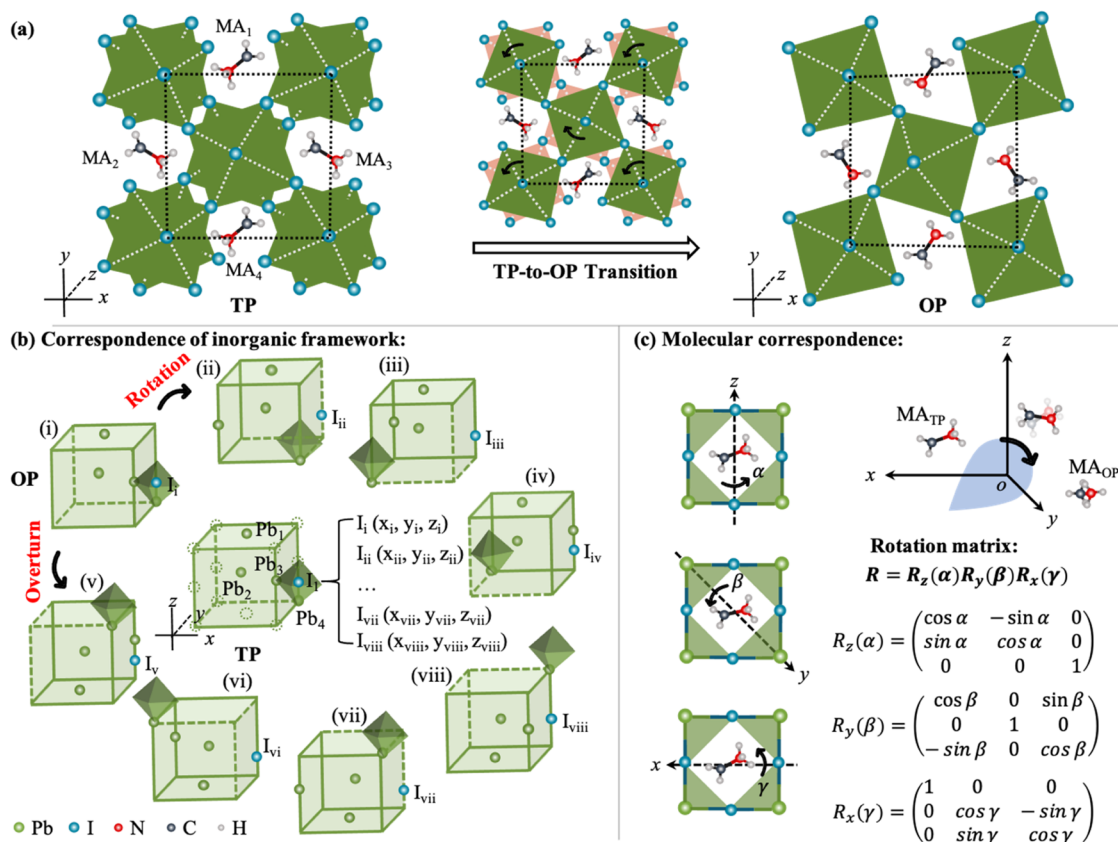


Figure 1. (a) Unit-cell structures of TP and OP and phase transition in between. In TP, the PbI_6^{4-} octahedra at the unit-cell corner are depicted in orange, while octahedra at the edge and body-centered positions of the unit cell are depicted in green. The transformational direction of PbI_6^{4-} octahedra is shown. (b) Schematic illustration of eight kinds of atomic coordinate correspondences between TP and OP, which involve the rotation (0° , 90° , 180° , and 270° in the xy -plane, generating configurations from i to iv) and the overturn (along the z -axis, generating configurations from v to viii) of the inorganic framework of OP. The inorganic framework consists of four PbI_3^- sublattices, where four Pb^{2+} ions occupy the corner, edge, face center, and body center of the unit cell, and I^- ions are at the corner of the PbI_6^{4-} octahedron. Four Pb^{2+} ions in the unit cell are depicted in solid circles, while other Pb^{2+} ions in the periodic slabs are depicted in dash circles. The coordinate correspondence of I^- in each structure is noted (I_i in TP and I_i – I_{viii} in OP). (c) Euler angles defining the rotation of MA^+ within the cavity along the z -axis (α), y -axis (β), and x -axis (γ). The correspondence between MA_{TP} (MA^+ in TP) and MA_{OP} (MA^+ in OP) is linked by the rotation matrix R . Color scheme: Pb, green; I, blue; N, red; C, black; and H, gray.

favorable phase transition pathway of HOIPs. In this work, by focusing on the TP-to-OP transition, we developed a revised nudged elastic band (NEB) method that allows us to better identify the possible nonsynergistic motions of inorganic/organic ions and revealed the low-temperature TP-to-OP transition mechanism. We clarified that it proceeds with a specific stepwise mode as a sequenced ensemble of Pb-I relaxation and molecular/axial rotations of MA^+ at an incredibly low effective barrier (0.08 eV/unit), which is an order of magnitude lower than that predicted by regular NEB and explains why and how the TP-to-OP transition can occur at low temperatures (<160 K). Moreover, the light absorption and charge transport properties were probed along the TP-to-OP transition and revealed the unexpected key photovoltaic role of organic MA^+ . Our findings may lay a basis for understanding the crystal-phase-dependent stability and the low-temperature efficiency of HOIPs.

RESULTS AND DISCUSSION

Outline of Phase Transition Pathways

Figure 1a shows the unit-cell structures of MAPbI_3 in the tetragonal and orthorhombic phases (Table S1) viewed along the z -axis, showing a framework of corner-sharing PbI_6^{4-} octahedron with MA^+ cation occupying each cavity enclosed

by the neighboring octahedra. The lattice parameters of TP were calculated to be $a = 8.89 \text{ \AA}$, $b = 8.87 \text{ \AA}$, $c = 13.20 \text{ \AA}$, and $\alpha = \beta = \gamma = 90^\circ$, and those of OP are $a = 8.98 \text{ \AA}$, $b = 8.74 \text{ \AA}$, $c = 12.96 \text{ \AA}$, and $\alpha = \beta = \gamma = 90^\circ$. The OP structure exhibits a regular arrangement of PbI_6^{4-} octahedra along the z -axis, while TP shows a twisted arrangement of these octahedra. Accordingly, these two structures can be visualized as transformed mainly by tilting PbI_6^{4-} octahedra at the edge- and body-centered positions of the unit cell and rotating the MA^+ cations within the cavities, while the PbI_6^{4-} octahedra at the unit-cell corner site almost remain motionless.

To explore the TP-to-OP transition kinetics, we first preliminarily outline the possible atomic coordinate correspondence linking TP with OP, where the minimum interatomic distance of inorganic framework³¹ was adopted for geometrical matching. Further, considering the symmetry of the tetragonal phase, particularly the structural similarity in a and b directions, eight correspondences of atomic coordinates linking TP with OP can be found (Figure 1b). Specifically, by overturn or 0° , 90° , 180° , and 270° rotation along the z -axis of OP, respectively, we can obtain eight OP equivalents exhibiting varying atomic positions of each component from the same viewing angle, leading to different TP-to-OP structural correspondences. Essentially, such a strategy takes different displacements of I^- /

Pb^{2+} and rotational angles of MA^+ into account, which can help cover the possible phase transition pathways as many as possible and thus facilitate locating the most favorable one. In addition, to describe the correspondence of MA^+ cations between TP and OP, the Euler angle was used to quantify the molecular and axial rotations of MA^+ with the rotation matrix. For example, as demonstrated in Figure 1c, MA_{TP} undergoes reorientation and ends at the corresponding positions in OP (MA_{OP} in Figure 1c), in which the transition from MA_{TP} to MA_{OP} can be obtained by three successive rotations around z , y , and x axes using the Euler angles (α , β , and γ) and rotation matrix $R = R_z(\alpha)R_y(\beta)R_x(\gamma)$. Following these recipes, we can build eight kinds of correspondences of inorganic and organic ions, and the displacements and rotation angles of all of the components in TP and OP can be completely determined in each one. The details of these outlined transformation pathways are given in Table S2 and Figure S1.

Stepwise NEB Method

Further, we developed a step-deciding technique incorporated with the NEB method, named as the sNEB method,³¹ permitting to fully explore the possible nonsynchronous movements of different components within MAPbI_3 and enabling multidirection sampling to better capture the MEP. As shown in Figure 2, the critical point of the sNEB method lies

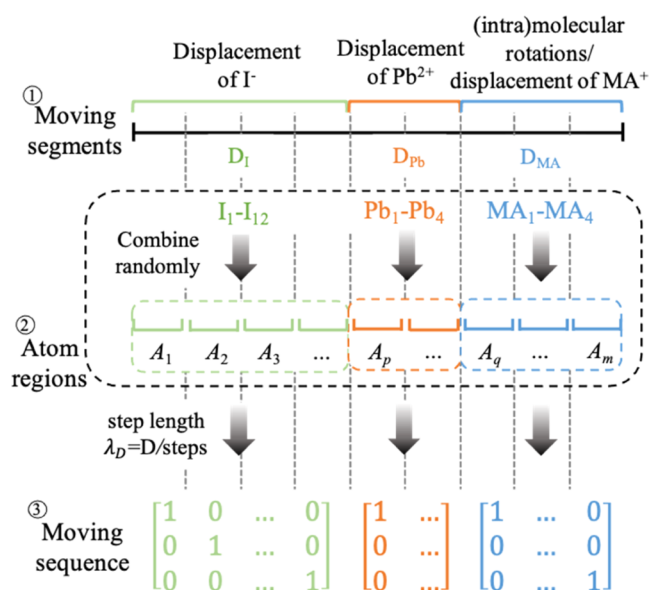


Figure 2. Basic concept of the sNEB method. D_I and D_{Pb} represent the displacements of I^- and Pb^{2+} , respectively, and D_{MA} represents the normalized change of both molecular displacement and the rotation angles. The matrix represents the possible moving sequence of atom regions, and the regions can move at varying step lengths and sequences.

in the step-deciding treatment: the separation of atom regions. We first split the overall transition process according to the transition behaviors of I^- , Pb^{2+} , and MA^+ , which involves the displacements of ions and the rotation of MA^+ . Considering the possibility of independent motions of ions, the same type of ions can further be divided into several regions ($A_1, \dots, A_p, \dots, A_m$), which allows ions to be randomly combined within a region and samples various moving patterns; ions in one region are allowed to move to their final positions in OP at various step lengths, while ions belonging to other regions remain motionless in this

process. The motions of all of the atom regions constitute complete ionic movements/rotations from TP to OP. By changing the atom combinations in these regions and their moving sequences, we are able to sample as many various transition patterns as possible, thereby taking into consideration all of the transformation pathways (Data S1 and Figure S2). Notably, the traditional NEB method usually adopts the linear interpolation of atomic positions to generate intermediate images, which cannot correctly describe the molecular rotation of MA^+ . sNEB additionally supports in generating images via linear interpolation of rotation angles of MA^+ by automatically invoking the rotation matrix, which guarantees the integrated expression of MA^+ rotation and displacement of the inorganic framework in exploiting the PES of TP-to-OP transition.

Phase Transition Mechanism

Considering all of the structural correspondences and the sNEB method, the minimum-energy phase-transition path can be gained and two kinds of characteristic mechanisms were identified (Figures S1 and 3a,b): (i) synergistic motions with activation energies of 0.41–0.51 eV (Paths 1–4); (ii) nonsynergistic motions with activation energies of 0.08–0.31 eV (Paths 5–8). Details of these transitions can be seen in Supporting Video Materials. Overall, such relatively large barriers in Paths 1–4 are reflected in that the $\text{I}^-/\text{Pb}^{2+}$ ions move with $\sim 110/140^\circ$ reorientation of MA^+ , while the nonsynergistic transitions are energetically more plausible, with multiple small barriers for independent motion of each component. As shown in Figure 3b,c, Path 5 is the optimal TP-to-OP transition pathway with an overall barrier of 0.08 eV, which proceeds stepwise via three specific stages: TP \rightarrow MS_1 , $\text{MS}_1 \rightarrow \text{MS}_2$, and $\text{MS}_2 \rightarrow$ OP.

Stage 1: TP \rightarrow MS_1 transition starts with the distortion of PbI_6^{4-} octahedra and I^- movements, accompanied by spontaneous $\sim 70^\circ$ rotations of adjacent MA_1/MA_2 . This process is exothermic with a barrier of 0.08 eV, resulting in a more stable intermediate MS_1 . Specifically, from TP to the transition state TS_1 (Figure 3c), the inorganic framework changes evidently, while all MA^+ remain nearly unchanged, indicating that the 0.08 eV barrier mainly comes from PbI_6^{4-} relaxation. In $\text{TS}_1 \rightarrow \text{MS}_1$, I^- ions continue to move to their final positions in OP, during which MA_1/MA_2 experience $\sim 70^\circ$ rotation in the yz -plane. As shown in Figure 3d, this small rotation of MA_1/MA_2 aims to suit the various $\text{N}-\text{H}\cdots\text{I}$ hydrogen bond interactions due to the reshaped cavities by tilted PbI_6^{4-} octahedra (Data S5).

Stages 2/3: Following the relaxation of the inorganic framework, MA_3/MA_4 proceed with stepwise large-angle reorientation within $\text{MS}_1 \rightarrow \text{MS}_2$ and $\text{MS}_2 \rightarrow$ OP, respectively, giving out-of-plane and in-plane (xy -plane) rotations of $\sim 110^\circ$ along the long-axis of cavity. In $\text{MS}_1 \rightarrow \text{MS}_2$, MA_3 starts with the molecular rotation in the yz -plane and ends with its C–N bond parallel to the xy -plane, giving rise to a 0.16 eV barrier. Finally, as MA_4 continues to rotate in the xy -plane, a small barrier (0.11 eV) appears to achieve $\text{MS}_2 \rightarrow$ OP transition (see details in Data S6).

Figure 3b depicts the potential energy profile of TP \rightarrow $\text{MS}_1 \rightarrow \text{MS}_2 \rightarrow$ OP transition (at 0 K), showing an energetically downhill process. Particularly, the TP \rightarrow MS_1 process is evidently heat-releasing, and the overall effective barrier can be identified as 0.08 eV/unit and the PbI_6^{4-} relaxation is the rate-limiting step. Compared to the commonly hypothesized synergistic mode, such a decoupled stepwise mechanism is

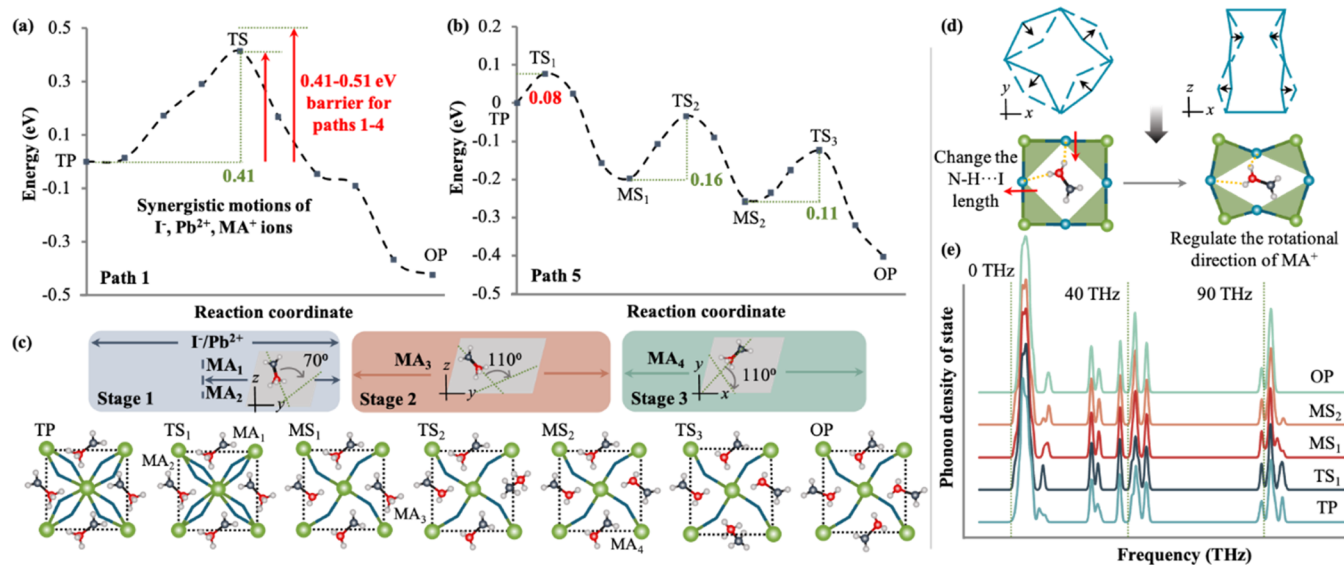


Figure 3. TP-to-OP transition mechanism and potential energy surface. (a, b) Energy profiles for Paths 1 and 5, respectively, where the intermediate/transition states (TS_1 , MS_1 , TS_2 , MS_2 , TS_3) and the activation barriers are noted. (c) Transition modes of I^-/Pb^{2+} ions and molecular rotations of four MA^+ cations in Path 5 viewed along the z -axis, where $MA_1/MA_2/MA_3/MA_4$ are indexed according to their motion sequence. (d) Schematic change of inorganic framework (mainly involving I^- vibration of ions) and the interplay between the cavity shape and rotational direction of MA^+ . (e) Total phonon density of states for each state during TP-to-OP transition.

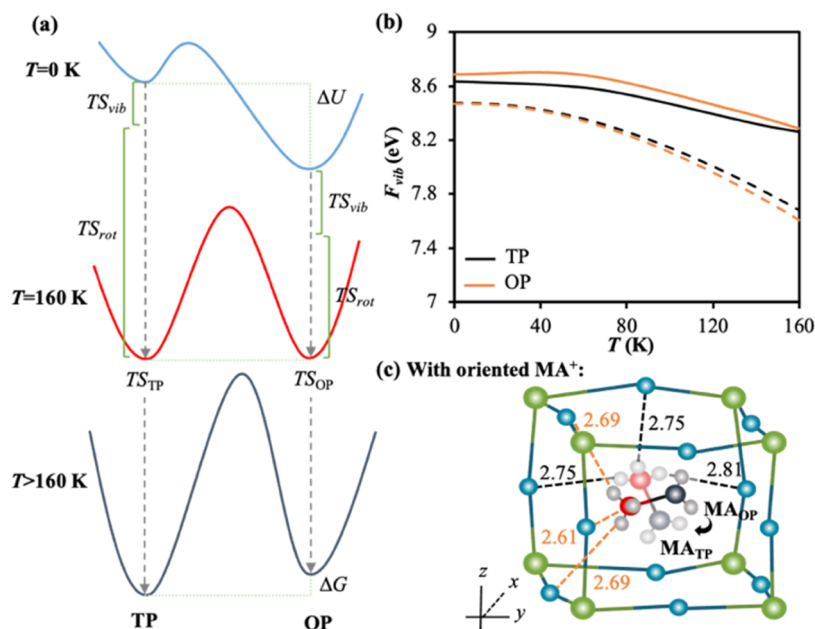


Figure 4. (a) Gibbs free energy landscape and entropy effects of TP-to-OP transition at elevated temperatures. The entropy contributions consist of lattice vibrational entropy (TS_{vib}) and rotational entropy (TS_{rot}). (b) Vibrational free energies with (solid line) and without (dash line) the anharmonic effect included, where the black and orange lines denote TP and OP, respectively. (c) Changes of N–H...I hydrogen bond lengths as the MA^+ rotates.

evidently more favorable. Noteworthy, by the lattice dynamic simulations, Figure 3e also provides the phonon density of states of each intermediate in this transition for further experimental validation (see details in Data S7, Figures S7 and S8).

Quantitatively, by comparing the structural features of eight paths, it was found that there is a strong dependence of the barriers on the degrees of coupled motion of different groups in $MAPbI_3$: the collective motions of inorganic/organic groups result in larger barriers (see details in Data S9 and Figure S9). We note that the large-angle reorientation of MA^+ is limited by the original stacking of PbI_6^{4-} octahedra in TP. In Path 5, the extra tension coming from Pb–I relaxation is largely released in

the TP \rightarrow MS_1 process, which results in weakened interplay between the inorganic framework and MA^+ and thus the cavity's expansion. This not only facilitates a relatively small rotation of MA_1/MA_2 but also contributes to the subsequent large-angle MA_3/MA_4 reorientation. In this regard, we propose that the nonsynergistic transition may be a common mechanism for HOIP materials. To the best of our knowledge, these results quantitatively present, arguably for the first time, a nonsynergistic mechanism for TP-to-OP transition with a low effective barrier, which rationalizes the easiness of TP-to-OP transition at low temperatures ($T \leq 160$ K) as observed experimentally.

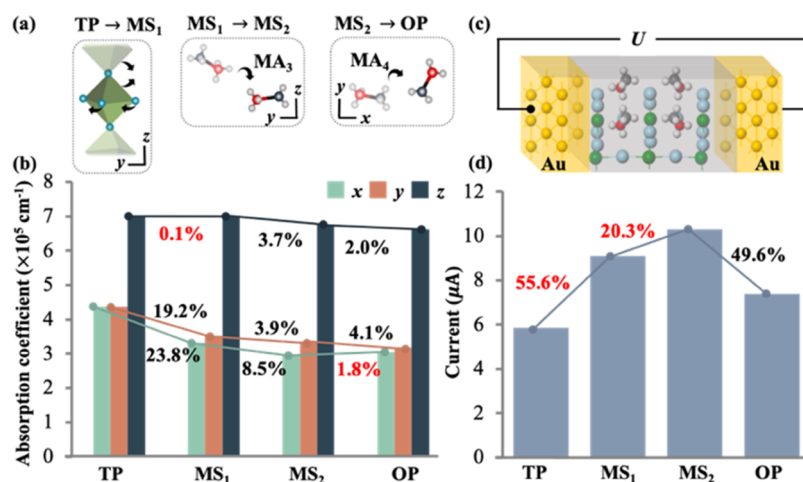


Figure 5. Photovoltaic properties of MAPbI₃ along TP-to-OP transition. (a) Motion modes of inorganic and organic groups along TP → MS₁ → MS₂ → OP transition. (b) Maximum light absorption coefficients of TP/MS₁/MS₂/OP along the x, y, z direction at a wavelength of 380 nm. (c) Diagram for the electronic transport calculation model, where MAPbI₃ is covered by two Au electrodes, and (d) the current changes at a bias voltage of 2 eV. Note: the differences in the absorption coefficient/current between structures (TP/MS₁/MS₂/OP) relate to the motions of inorganic displacement, MA₃ and MA₄ reorientation, respectively, where red numbers denote the percentage increase and black represents the percentage decrease by taking TP as the reference.

Inferred from this potential-energy landscape, on the one hand, some strategies may be plausible to maintain the TP stability in low-temperature applications:^{32–34} (i) improving the inflexibility of the inorganic framework to inhibit the phase-transition initiation step; (ii) introducing the larger-sized organic cation to weaken the large-angle reorientation. Noticeably, recent experiments have verified that large-sized organic ions could enter the bulk perovskite lattice and the introduction of these cations can improve the stability of the single crystal, despite being more often understood from the perspective of tuning the tolerance factor of bulk perovskite.^{35–38} In this regard, our results give an atomic level evidence in terms of slowing down the phase-transition kinetics to guard the stability of the hybrid perovskite. In addition to the bulk phase stability itself, the phase transition or structural deformation could be often triggered at the surface, edge, or the defect site, and thus the practical improvements to stabilize the materials in many cases relate to the passivation of surfaces and grain boundaries (e.g., coating with the organic molecule layer) or the interface stabilization effect confined by the substrate, which correspond to the cases of thin films or the nanocrystal form of perovskite.^{39,40}

On the other hand, we can further understand the origin of temperature-dependent phase transition; at $T \leq 160$ K, TP is easily transformed into OP, while the transition would be relatively hindered when $T > 160$ K. At non-zero temperatures, the lattice vibration and rotation of MA⁺ are activated and could lower the free energies of TP and OP, as illustrated in Figure 4a. The harmonic and anharmonic lattice vibration contributions were calculated to be -0.07 and 0.10 eV, respectively, at $T = 160$ K for the free energy change from TP to OP (Figure 4b); in combination with the potential energy difference (-0.40 eV) between the two phases, one can speculate that the presence of rotational entropy regulates the phase equilibrium at 160 K. As Figure 4c describes, the H-bond strength in OP is stronger than that in TP, which leads to larger vibration frequencies and entropy contribution, but the degree of rotation freedom of MA⁺ would be more inhibited. The rotational entropy lowers the free energy of TP well below the OP and becomes more pronounced

at $T > 160$ K, which arguably explains the relative stability of TP at room temperature and thus demonstrates the dominant effect of rotational entropy of organic cations in adjusting TP-to-OP transition at elevated temperatures.

Structure-Dependent Photovoltaic Properties

With the TP → OP transition mechanism identified, it could be worth probing the structure-induced property change (i.e., the basic structure–property relationship) and further understand the structural origin of phase-dependent photovoltaic properties of MAPbI₃ arising from the relaxation/orientation of the inorganic and organic ions in the low-temperature condition. Figure 5a,b show the maximum light absorption coefficients (α_{\max}) in the near-visible light region. One can see that α_{\max} is gradually decreased along the phase transition and dominated by the relaxation of PbI₆⁴⁻ (corresponding to TP → MS₁ transition). This could relate to the fact that I⁻/Pb²⁺ contributes greatly to the electronic band-edge. Approximately, the overall light absorption is weakened by 23.8% during the Pb-I relaxation. Moreover, the anisotropic rotations of MA₃ and MA₄ also affect light absorption, despite the weakened influence relative to the inorganic motions. α_{\max} respectively, decreases by nearly 8.5% and 4.1% during these two processes. Noticeably, the contributions of charge transport property for TP → MS₁ and MS₁ → MS₂ transitions are opposite to those of the near-visible light absorption ability (Figure 5c,d); the inorganic framework relaxation and MA₃ rotation lead to an overall reduction in the light absorption but significant improvement in the charge transport, in which the current increases by 55.6% and 20.3%, respectively. This may, to some extent, yield a balanced and help to guard relatively steady photovoltaic performance from TP to MS₂. Differently, both properties show decreasing trends in the final MS₂ → OP step. This demonstrates that the motion of the last organic cation, i.e., MA₄ rotation, would play a generally adverse role and drop drastically the performance of solar cells. These findings emphasize the importance of metastable state MS₂; conceptually, MA₄ may guard the photovoltaic performance of MAPbI₃ by controlling the in-plane molecular rotation. Therefore, one can speculate that introducing even low content (<25%) of

large-sized organic cations could be advantageous to maintain MAPbI₃ at TP or MS₂ states and thus quasi-stable performance, which essentially agrees with the very recent experimental finding⁴¹ that a small amount of dimethylamine substitution improves structural stability and photovoltaic properties of MAPbI₃.

CONCLUSIONS

In summary, we elaborated on the tetragonal-to-orthorhombic phase transition kinetics of MAPbI₃ via a new sNEB method. The kinetically most plausible mechanism was quantitatively identified, where the motion of inorganic octahedra and large-angle reorientations of organic cations are decoupled to three sequential transformation stages. The uncovered potential energy landscape explains the easiness of TP-to-OP transition at extremely low temperatures (<160 K) and constitutes a basis for understanding the temperature-dependent phase transition of MAPbI₃ at elevated temperatures. Enabled by such a stepwise mechanism, the functionalities of inorganic and organic ions in affecting the photovoltaic performance of MAPbI₃ were evaluated along the phase-transition process. Unexpectedly, we found that there may exist a hysteresis effect of overall photovoltaic efficiency in the structural phase transition, and the in-plane rotation of MA⁺ cation (corresponding to the last stage of TP-to-OP transition) could help to guard the photovoltaic performance of MAPbI₃. We expect that the insights obtained are crucial for understanding the structural transition kinetics and maintaining the performances of MAPbI₃.

METHODS

Density Functional Theory (DFT) Calculations

The stable tetragonal bulk unit ($a = 8.89 \text{ \AA}$, $b = 8.87 \text{ \AA}$, $c = 13.20 \text{ \AA}$, $\alpha = \beta = \gamma = 90^\circ$) and orthorhombic bulk unit ($a = 8.98 \text{ \AA}$, $b = 8.74 \text{ \AA}$, $c = 12.96 \text{ \AA}$, $\alpha = \beta = \gamma = 90^\circ$), each containing 24 H, 4 C, 4 N, 12 I, and 4 Pb atoms, were used. Total energy calculations were carried out with the Perdew–Burke–Ernzerhof (PBE) functional using the Vienna *Ab initio* Simulation Package (VASP).⁴² To correctly describe the geometric and electronic structure of MAPbI₃, the spin–orbit coupling (SOC) together with the DFT+*U* (I: 8 eV, Pb: 9 eV) approach was used.^{43,44} The DFT-D3 method^{45,46} also was employed to describe the weak interaction in the hybrid perovskite. The energy cutoff of the plane wave basis set was set as 450 eV. The Brillouin zone was sampled using the Monkhorst–Pack scheme with a $2 \times 2 \times 2$ *k*-point mesh in NEB, a $5 \times 5 \times 3$ *k*-point mesh for TP, and a $5 \times 4 \times 5$ for OP in lattice dynamics calculations. Optimized structures were obtained when the forces are below 0.05 eV/Å.

Ab Initio Lattice Dynamic Calculations

Ab initio lattice dynamics calculations were performed to obtain the vibrational modes. The harmonic term of lattice vibration was examined with the frozen phonon approximation, while the cubic and quartic terms of anharmonicity were then calculated with the self-consistent phonon theory, using the ALAMODE package^{47,48} to obtain the anharmonic vibrational effect.

Absorption Coefficient

According to the equation

$$\alpha(\omega) = (2\omega)^{1/2} [(\epsilon_1(\omega)^2 + \epsilon_2(\omega)^2)^{1/2} - \epsilon_1(\omega)]^{1/2} \quad (1)$$

the frequency-dependent absorption coefficient $\alpha(\omega)$ can be quantitatively calculated and understood from the variation of real ($\epsilon_1(\omega)$) and imaginary ($\epsilon_2(\omega)$) components of the dielectric functions.^{49,50}

Charge Transport

Transport properties were computed with nonequilibrium Green's functions as implemented in TranSIESTA,^{51,52} which allows for simulations with open boundary conditions. The system is composed of three regions: left Au-electrode, right Au-electrode, and the central scattering region, where the structure found in the tetragonal–orthorhombic structural transformation is inserted to screen out the perturbation of the scatter. In the calculations, GGA/PBE⁴² were used along with the nonconserving pseudopotentials of the Troullier–Martins type⁵³ for the description of the core electrons. The valence wave functions were described by a double- ξ polarized basis set (DZP) of finite-range numerical pseudoatomic orbitals. In all cases, an energy cutoff of 200 Ry for real-space mesh size was used.

ASSOCIATED CONTENT

Supporting Information

The Supporting Information is available free of charge at <https://pubs.acs.org/doi/10.1021/jacsau.3c00060>.

Additional theoretical methods and details in Supporting Data S1–S11, Figure S1–S10, and Tables S1–S3, including the descriptions of the sNEB method, TP/OP structures, phase transition pathways, phonon analysis, and photovoltaic properties (PDF)

Additional phase transition animations in Supporting Video Materials (ZIP)

AUTHOR INFORMATION

Corresponding Author

Haifeng Wang – Key Laboratory for Advanced Materials, Center for Computational Chemistry and Research Institute of Industrial Catalysis, School of Chemistry and Molecular Engineering, East China University of Science and Technology, Shanghai 200237, P. R. China; orcid.org/0000-0002-6138-5800; Email: hfwang@ecust.edu.cn

Authors

Jiawei Wu – Key Laboratory for Advanced Materials, Center for Computational Chemistry and Research Institute of Industrial Catalysis, School of Chemistry and Molecular Engineering, East China University of Science and Technology, Shanghai 200237, P. R. China

Jianfu Chen – Key Laboratory for Advanced Materials, Center for Computational Chemistry and Research Institute of Industrial Catalysis, School of Chemistry and Molecular Engineering, East China University of Science and Technology, Shanghai 200237, P. R. China

Complete contact information is available at: <https://pubs.acs.org/10.1021/jacsau.3c00060>

Author Contributions

†J.W. and J.C. contributed equally to this work.

Author Contributions

CRediT: **Jiawei Wu** data curation, formal analysis, investigation, writing-original draft; **Jianfu Chen** data curation, investigation, methodology; **Haifeng Wang** conceptualization, project administration, supervision.

Notes

The authors declare no competing financial interest.

ACKNOWLEDGMENTS

This project was supported by the National Key R&D Program of China (2021YFA1500700, 2018YFA0208602), NSFC (92045303, 21703067, 22202069, 21873028), and the Fundamental Research Funds for the Central Universities. J.W.W. thanks the China Scholarship Council for sponsorship.

REFERENCES

- (1) Bella, F.; Griffini, G.; Correa-Baena, J. P.; Saracco, G.; Grätzel, M.; Hagfeldt, A.; Turri, S.; Gerbaldi, C. Improving efficiency and stability of perovskite solar cells with photocurable fluoropolymers. *Science* **2016**, *354*, 203–206.
- (2) Saliba, M.; Matsui, T.; Domanski, K.; Seo, J. Y.; Ummadisingu, A.; Zakeeruddin, S. M.; Correa-Baena, J. P.; Tress, W. R.; Abate, A.; Hagfeldt, A.; Grätzel, M. Incorporation of rubidium cations into perovskite solar cells improves photovoltaic performance. *Science* **2016**, *354*, 206–209.
- (3) Yang, W. S.; Noh, J. H.; Jeon, N. J.; Kim, Y. C.; Ryu, S.; Seo, J.; Seok, S. I. High-performance photovoltaic perovskite layers fabricated through intramolecular exchange. *Science* **2015**, *348*, 1234–1237.
- (4) Shin, S. S.; Yeom, E. J.; Yang, W. S.; Hur, S.; Kim, M. G.; Im, J.; Seo, J.; Noh, J. H.; Seok, S. I. Colloidally prepared La-doped BaSnO₃ electrodes for efficient, photostable perovskite solar cells. *Science* **2017**, *356*, 167–171.
- (5) National Renewable Energy Laboratory. Best research-cell efficiencies chart. <https://www.nrel.gov/pv/cell-efficiency.html> (accessed November, 2022).
- (6) Aristidou, N.; Eames, C.; Sanchez-Molina, I.; Bu, X.; Kosco, J.; Islam, M. S.; Haque, S. A. Fast oxygen diffusion and iodide defects mediate oxygen-induced degradation of perovskite solar cells. *Nat. Commun.* **2017**, *8*, No. 15218.
- (7) Divitini, G.; Cacovich, S.; Matteocci, F.; Cinà, L.; Di Carlo, A.; Ducati, C. In situ observation of heat-induced degradation of perovskite solar cells. *Nat. Energy* **2016**, *1*, No. 15012.
- (8) Yang, J.; Siempelkamp, B. D.; Liu, D.; Kelly, T. L. Investigation of CH₃NH₃PbI₃ degradation rates and mechanisms in controlled humidity environments using in situ techniques. *ACS Nano* **2015**, *9*, 1955–1963.
- (9) Bryant, D.; Aristidou, N.; Pont, S.; Sanchez-Molina, I.; Chotchanangachaval, T.; Wheeler, S.; Durrant, J. R.; Haque, S. A. Light and oxygen induced degradation limits the operational stability of methylammonium lead triiodide perovskite solar cells. *Energy Environ. Sci.* **2016**, *9*, 1655–1660.
- (10) Chen, S.; Zhang, X.; Zhao, J.; Zhang, Y.; Kong, G.; Li, Q.; Li, N.; Yu, Y.; Xu, N.; Zhang, J.; Liu, K.; Zhao, Q.; Cao, J.; Feng, J.; Li, X.; Qi, J.; Yu, D.; Li, J.; Gao, P. Atomic scale insights into structure instability and decomposition pathway of methylammonium lead iodide perovskite. *Nat. Commun.* **2018**, *9*, No. 4807.
- (11) Bernard, G. M.; Wasylishen, R. E.; Ratcliffe, C. I.; Tersikh, V.; Wu, Q.; Buriak, J. M.; Hauger, T. Methylammonium cation dynamics in methylammonium lead halide perovskites: A solid-state NMR perspective. *J. Phys. Chem. A* **2018**, *122*, 1560–1573.
- (12) Mattoni, A.; Filippetti, A.; Saba, M. I.; Delugas, P. Methylammonium rotational dynamics in lead halide perovskite by classical molecular dynamics: The role of temperature. *J. Phys. Chem. C* **2015**, *119*, 17421–17428.
- (13) Whitfield, P. S.; Herron, N.; Guise, W. E.; Page, K.; Cheng, Y. Q.; Milas, I.; Crawford, M. K. Structures, phase transitions and tricritical behavior of the hybrid perovskite methyl ammonium lead iodide. *Sci. Rep.* **2016**, *6*, No. 35685.
- (14) Ong, K. P.; Goh, T. W.; Xu, Q.; Huan, A. Mechanical origin of the structural phase transition in methylammonium lead iodide CH₃NH₃PbI₃. *J. Phys. Chem. Lett.* **2015**, *6*, 681–685.
- (15) Baikie, T.; Fang, Y.; Kadro, J. M.; Schreyer, M.; Wei, F.; Mhaisalkar, S. G.; Graetzel, M.; White, T. J. Synthesis and crystal chemistry of the hybrid perovskite (CH₃NH₃)PbI₃ for solid-state sensitized solar cell applications. *J. Mater. Chem. A* **2013**, *1*, S628–S641.
- (16) Antonietta, L. M.; Hummelen, J. C. Perovskites under the Sun. *Nat. Mater.* **2013**, *12*, 1087–1089.
- (17) Knop, O.; Wasylishen, R. E.; White, M. A.; Cameron, T. S.; Oort, M. J. V. Alkylammonium lead halides. Part 2. CH₃NH₃PbX₃ (X = Cl, Br, I) perovskites: Cuboctahedral halide cages with isotropic cation reorientation. *Can. J. Chem.* **1990**, *68*, 412–422.
- (18) Shimamura, K.; Hakamata, T.; Shimojo, F.; Kalia, R. K.; Nakano, A.; Vashishta, P. Rotation mechanism of methylammonium molecules in organometal halide perovskite in cubic phase: An ab initio molecular dynamics study. *J. Chem. Phys.* **2016**, *145*, No. 224503.
- (19) Li, J.; Bouchard, M.; Reiss, P.; Aldakov, D.; Pouget, S.; Demadrille, R.; Aumaitre, C.; Frick, B.; Djurado, D.; Rossi, M.; Rinke, P. Activation energy of organic cation rotation in CH₃NH₃PbI₃ and CD₃NH₃PbI₃: quasi-elastic neutron scattering measurements and first-principles analysis including nuclear quantum effects. *J. Phys. Chem. Lett.* **2018**, *9*, 3969–3977.
- (20) Qiao, W. C.; Wu, J.; Zhang, R.; Ou-Yang, W.; Chen, X.; Yang, G.; Chen, Q.; Wang, X. L.; Wang, H. F.; Yao, Y. F. In situ NMR investigation of the photoresponse of perovskite crystal. *Matter* **2020**, *3*, 2042–2054.
- (21) Saidi, W. A.; Choi, J. J. Nature of the cubic to tetragonal phase transition in methylammonium lead iodide perovskite. *J. Chem. Phys.* **2016**, *145*, No. 144702.
- (22) Schuck, G.; Többsen, D. M.; Koch-Müller, M.; Efthimiopoulos, L.; Schorr, S. Infrared spectroscopic study of vibrational modes across the orthorhombic-tetragonal phase transition in methylammonium lead halide single crystals. *J. Phys. Chem. C* **2018**, *122*, 5227–5237.
- (23) Jinnouchi, R.; Lahnsteiner, J.; Karsai, F.; Kresse, G.; Bokdam, M. Phase transitions of hybrid perovskites simulated by machine-learning force fields trained on the fly with Bayesian inference. *Phys. Rev. Lett.* **2019**, *122*, No. 225701.
- (24) Bonadio, A.; E, C. A., Jr; Sabino, F. P.; Sombrio, G.; de Paula, V. G.; Ferreira, F. F.; Janotti, A.; Dalpian, G. M.; Souza, J. A. Entropy-driven stabilization of the cubic phase of MAPbI₃ at room temperature. *J. Mater. Chem. A* **2021**, *9*, 1089–1099.
- (25) Deretzis, I.; La, M. A. Exploring the orthorhombic-tetragonal phase transition in CH₃NH₃PbI₃: The role of atom kinetics. *Nanoscale* **2017**, *9*, 5896–5903.
- (26) Wei, W.; Li, W.; Butler, K. T.; Feng, G.; Howard, C. J.; Carpenter, M. A.; Lu, P.; Walsh, A.; Cheetham, A. K. An unusual phase transition driven by vibrational entropy changes in a hybrid organic–inorganic perovskite. *Angew. Chem., Int. Ed.* **2018**, *57*, 8932–8936.
- (27) Chen, T.; Foley, B. J.; Park, C.; Brown, C. M.; Harriger, L. W.; Lee, J.; Ruff, J.; Yoon, M.; Choi, J. J.; Lee, S. Entropy-driven structural transition and kinetic trapping in formamidinium lead iodide perovskite. *Sci. Adv.* **2016**, *2*, No. 1601650.
- (28) Chen, T.; Chen, W. L.; Foley, B. J.; Ruff, J.; Lee, J.; Peter Ko, J. Y.; Brown, C. M.; Harriger, L. W.; Zhang, D.; Park, C.; Yoon, M.; Chang, Y. M.; Choi, J. J.; Lee, S. Origin of long lifetime of band-edge charge carriers in organic–inorganic lead iodide perovskites. *Proc. Natl. Acad. Sci. U.S.A.* **2017**, *114*, 7519–7524.
- (29) Szafranski, M.; Katrusiak, A. Mechanism of pressure-induced phase transitions, amorphization, and absorption-edge shift in photo-voltaic methylammonium lead iodide. *J. Phys. Chem. Lett.* **2016**, *7*, 3458–3466.
- (30) Keshavarz, M.; Ottesen, M.; Wiedmann, S.; Wharmby, M.; Küchler, R.; Yuan, H.; Debroye, E.; Steele, J. A.; Martens, J.; Hussey, N. E.; Bremholm, M.; Roeffaers, M. B. J.; Hofkens, J. Tracking structural phase transitions in lead-halide perovskites by means of thermal expansion. *Adv. Mater.* **2019**, *31*, No. 1900521.
- (31) Jia, M.; Chen, J.; Wang, H. (2 × 1) reconstruction mechanism of rutile TiO₂(011) surface. *ACS Nano* **2023**, *17*, 3549–3556.
- (32) Jacobsson, T. J.; Tress, W.; Correa-Baena, J. P.; Edvinsson, T.; Hagfeldt, A. Room temperature as a goldilocks environment for CH₃NH₃PbI₃ perovskite solar cells: The importance of temperature on device performance. *J. Phys. Chem. C* **2016**, *120*, 11382–11393.
- (33) Zhang, H.; Qiao, X.; Shen, Y.; Moehl, T.; Zakeeruddin, S. M.; Grätzel, M.; Wang, M. Photovoltaic behaviour of lead methylammo-

nium triiodide perovskite solar cells down to 80 K. *J. Mater. Chem. A* **2015**, *3*, 11762–11767.

(34) Osherov, A.; Hutter, E. M.; Galkowski, K.; Brenes, R.; Maude, D. K.; Nicholas, R. J.; Plochocka, P.; Bulović, V.; Savenije, T. J.; Stranks, S. D. The impact of phase retention on the structural and optoelectronic properties of metal halide perovskites. *Adv. Mater.* **2016**, *28*, 10757–10763.

(35) Li, Z.; Yang, M.; Park, J. S.; Wei, S. H.; Berry, J. J.; Zhu, K. Stabilizing perovskite structures by tuning tolerance factor: Formation of formamidinium and cesium lead iodide solid-state alloys. *Chem. Mater.* **2016**, *28*, 284–292.

(36) Jiang, Q.; Zhao, Y.; Zhang, X.; Yang, X.; Chen, Y.; Chu, Z.; Ye, Q.; Li, X.; Yin, Z.; You, J. Surface passivation of perovskite film for efficient solar cells. *Nat. Photonics* **2019**, *13*, 460–466.

(37) Francisco-López, A.; Charles, B.; Isabel Alonso, M.; Garriga, M.; Campoy-Quiles, M.; Weller, M. T.; Goñi, A. R. Phase diagram of methylammonium/formamidinium lead iodide perovskite solid solutions from temperature-dependent photoluminescence and raman spectroscopies. *J. Phys. Chem. C* **2020**, *124*, 3448–3458.

(38) Senno, M.; Tinte, S. Mixed formamidinium–methylammonium lead iodide perovskite from first-principles: Hydrogen-bonding impact on the electronic properties. *Phys. Chem. Chem. Phys.* **2021**, *23*, 7376–7385.

(39) Jung, M.; Shin, T. J.; Seo, J.; Kim, G.; Seok, S. I. Structural features and their functions in surfactant-armoured methylammonium lead iodide perovskites for highly efficient and stable solar cells. *Energy. Environ. Sci.* **2018**, *11*, 2188–2197.

(40) Ye, F.; Zhang, S.; Warby, J.; Wu, J.; Gutierrez, E.; Lang, F.; Shan, S.; Saglamkaya, E.; Sun, B.; Zu, F.; Shoaee, S.; Wang, H.; Stiller, B.; Neher, D.; Zhu, W.; Stolterfoht, M.; Wu, Y. Overcoming C60-induced interfacial recombination in inverted perovskite solar cells by electron-transporting carborane. *Nat. Commun.* **2022**, *13*, No. 7454.

(41) Qiao, W. C.; Liang, J. Q.; Dong, W.; Ma, K.; Wang, X. L.; Yao, Y. F. Formamidinium lead triiodide perovskites with improved structural stabilities and photovoltaic properties obtained by ultratrace dimethylamine substitution. *NPG Asia Mater.* **2022**, *14*, No. 49.

(42) Kresse, G.; Furthmüller, J. Efficiency of *ab-initio* total energy calculations for metals and semiconductors using a plane-wave basis set. *Comput. Mater. Sci.* **1996**, *6*, 15–50.

(43) Peng, C.; Chen, J.; Wang, H.; Hu, P. First-principles insight into the degradation mechanism of CH₃NH₃PbI₃ perovskite: Light-induced defect formation and water dissociation. *J. Phys. Chem. C* **2018**, *122*, 27340–27349.

(44) Peng, C.; Wang, J.; Wang, H.; Hu, P. Unique trapped dimer state of the photogenerated hole in hybrid orthorhombic CH₃NH₃PbI₃ perovskite: Identification, origin, and implications. *Nano Lett.* **2017**, *17*, 7724–7730.

(45) Grimme, S.; Ehrlich, S.; Goerigk, L. Effect of the damping function in dispersion corrected density functional theory. *J. Comput. Chem.* **2011**, *32*, 1456–1465.

(46) Grimme, S.; Antony, J.; Ehrlich, S.; Krieg, H. A consistent and accurate *ab initio* parametrization of density functional dispersion correction (DFT-D) for the 94 elements H–Pu. *J. Chem. Phys.* **2010**, *132*, No. 154104.

(47) Tadano, T.; Gohda, Y.; Tsuneyuki, S. Anharmonic force constants extracted from first-principles molecular dynamics: Applications to heat transfer simulations. *J. Phys.: Condens. Matter.* **2014**, *26*, No. 225402.

(48) Tadano, T.; Tsuneyuki, S. Self-consistent phonon calculations of lattice dynamical properties in cubic SrTiO₃ with first-principles anharmonic force constants. *Phys. Rev. B* **2015**, *92*, No. 054301.

(49) Ambrosch-Draxl, C.; Sofo, J. O. Linear optical properties of solids within the full-potential linearized augmented planewave method. *Comput. Phys. Commun.* **2006**, *175*, 1–14.

(50) Dar, S. A.; Sharma, R.; Srivastava, V.; Sakalle, U. K. Investigation on the electronic structure, optical, elastic, mechanical, thermodynamic and thermoelectric properties of wide band gap semiconductor double perovskite Ba₂InTaO₆. *RSC Adv.* **2019**, *9*, 9522–9532.

(51) Papior, N.; Lorente, N.; Frederiksen, T.; García, A.; Brandbyge, M. Improvements on non-equilibrium and transport Green function techniques: The next-generation transiesta. *Comput. Phys. Commun.* **2017**, *212*, 8–24.

(52) Brandbyge, M.; Mozos, J. L.; Ordejón, P.; Taylor, J.; Stokbro, K. Density-functional method for nonequilibrium electron transport. *Phys. Rev. B* **2002**, *65*, No. 165401.

(53) Troullier, N.; Martins, J. L. Efficient pseudopotentials for plane-wave calculations. *Phys. Rev. B* **1991**, *43*, 1993–2006.